Advances in Differential Equations and Control Processes 2026, 33(3), 4327.
doi: https://doi.org/10.59400/adecp4327

Article

Channeling paths identification and mitigation by using integrated profile control and flooding based on meshless connection element method

Wei Yong[1,2], Zhijie Wei[1,2], Jian Zhang[1,2], Wensheng Zhou[1,2], Yuyang Liu[1,2], Wentao Zhan[3,4,*], Wei Liu[3,4], Yixin Zhang[4], Jiaxu Mei[4]

[1] State Key Laboratory of Offshore Oil and Gas Exploitation, Beijing 100028, China
[2] CNOOC Research Institute Co. Ltd., Beijing 100028, China
[3] Western Research Institute, Yangtze University, Karamay 834000, China
[4] State Key Laboratory of Low Carbon Catalysis and Carbon Dioxide Utilization, Yangtze University, Wuhan 430100, China
*** Corresponding authors:** Wentao Zhan, zhanwt1996@163.com

CITATION

Yong W, Wei Z, Zhang J, et al. Channeling paths identification and mitigation by using integrated profile control and flooding based on meshless connection element method. JAdvances in Differential Equations and Control Processes. 2026; 33(3): 4327. https://doi.org/10.59400/adecp4327

ARTICLE INFO

Received: 26 April 2026
Revised: 30 June 2026
Accepted: 6 July 2026
Available online: 17 July 2026

COPYRIGHT

Copyright © 2026 Author(s). *Advances in Differential Equations and Control Processes* is published by Academic Publishing Pte Ltd. This work is licensed under the Creative Commons Attribution (CC BY) license. https://creativecommons.org/licenses/by/4.0/

Abstract: Addressing the challenge of quantitatively identifying deep thief zones in mature oilfields during the high water-cut stage, this study proposes a robust quantitative characterization model for thief channels based on the non-Euclidean, meshless Connection Element Method (CEM) to directly guide in-depth fluid diversion and integrated profile control and flooding treatments through automated flow path tracking rooted in a directed-graph depth-first search algorithm. To systematically capture the complex subsurface topological network, a comprehensive multi-parameter connectivity parameter system was constructed by integrating key dynamic indicators, including connection conductivity, connection volume, and path splitting coefficients. By dynamically coupling these parameters with the field-wide Lorentz coefficient, a dimensionless channeling factor was defined to establish a rigorous four-level quantitative standard—ranging from extreme channeling to matrix seepage—thereby successfully advancing preferential pathway evaluation from qualitative inference to spatial grading and precise localization. Quantitative validation against conventional commercial grid-based compositional simulators demonstrates the superior fidelity and performance forecasting efficiency of the proposed method: the CEM framework achieves an exceptionally accurate water-cut prediction Root Mean Square Error (RMSE) of approximately 3.8%. Crucially, by abstracting continuous domains into streamlined networks, it drastically compresses structural degrees of freedom, successfully accelerating the operational execution runtime from 7.3 s to a mere 1.6 s. Ultimately, this work provides a computationally highly efficient, physically sound novel approach for the reliable mapping and graded quantification of deep dominant channeling pathways in mature heterogeneous oilfields.

Keywords: meshless connection element method; integrated profile control; identification of channeling paths

1. Introduction

Water flooding is the primary method to maintain formation energy and improve crude oil recovery. However, in the late stage of high water-cut development, combined with reservoir heterogeneity, anisotropy, and long-term fluid scouring, highly conductive preferential flow pathways [1, 2] easily form inside the reservoir. Injection water circulates inefficiently along these low-resistance paths, greatly reducing sweep efficiency, while a large amount of residual oil remains trapped in

low-permeability matrix and is difficult to produce. Therefore, implementing in-depth fluid diversion technologies integrating "plugging, profile control, and flooding" (integrated profile control and flooding) has become an inevitable choice. Through physicochemical effects of chemical agents, these technologies achieve "viscosity increase and permeability reduction," aiming to block high-conductivity channels and redirect fluid flow toward oil-rich regions [3, 4]. Nevertheless, the key to successful profile control and flooding lies in effectively identifying the spatial topology of channeling pathways and quantitatively evaluating their channeling intensity, so as to formulate differentiated targeted control strategies.

At present, methods for identifying inter-well connectivity are mainly divided into field monitoring analysis and data-driven model analysis, covering five core approaches: logging analysis, chemical analysis, well test analysis, tracer analysis, and injection–production dynamic analysis. Each method has specific applications in qualitative connectivity judgment, quantitative characterization, and preferential pathway identification. Field monitoring methods directly reflect formation connectivity based on measured field data. Among them, logging analysis determines connectivity through parameter calculation and curve comparison using conventional logging and image logging techniques. It is simple to operate but can only reflect static geological characteristics [5,6]. Chemical analysis mainly relies on crude oil chromatographic fingerprint technology, judging fluid connectivity by similarity of oil sample chromatographic features. It offers high accuracy but suffers from high cost, limiting large-scale application [7]. Well test analysis adopts interference testing and pulse testing, inverting connectivity from pressure and production dynamics. Its results are reliable yet require heavy testing workloads and high costs [8, 9]. Tracer analysis evaluates connectivity through tracer monitoring between injection and production wells. It has high precision and strong targeting, suitable for reservoirs with complex geology [10, 11]. In recent years, data-driven models based on injection–production dynamic data have become a research hotspot. Representative methods include the capacitance-resistance model (CRM) [12, 13] and the multiple linear regression model (MLR). Without additional field tests, these methods only use routine injection, production, and pressure data to obtain connectivity conductivity, splitting coefficients, and other indicators through mathematical inversion, realizing quantitative characterization of connectivity [14–17]. They effectively compensate for the shortcomings of traditional monitoring methods, such as long cycles and insufficient full-domain coverage, and have become mainstream evaluation technologies. Traditional injection-production response analysis generally ignores seepage physical mechanisms and dynamic time lag effects between wells, relying only on simple mathematical correlations. Thus, it cannot describe complex seepage behaviors in heterogeneous reservoirs, leading to low characterization accuracy and poor physical rationality.

To overcome insufficient physical mechanism description in traditional connectivity models, Zhao et al. proposed a meshless data-driven model for conventional water-flooded reservoirs, namely the Inter-well Network Simulation Model (INSIM). This model simplifies complex three-dimensional reservoir flow into

one-dimensional inter-well connectivity networks. It uses two lumped parameters, conductivity and connected volume, to characterize inter-well flow pathways, and combines Buckley-Leverett (BL) theory to semi-analytically solve water saturation distribution [18]. Compared with conventional grid-based models, INSIM contains far fewer parameters, increases computational efficiency by hundreds of times while maintaining prediction accuracy, and enables rapid history matching of production performance. Subsequently, to further improve characterization capability for complex flows, the INSIM system has been continuously expanded and improved. The INSIM-FT model introduces a front-tracking algorithm and significantly improves water cut prediction accuracy [19]. Guo and Reynolds proposed INSIM-FT-3D, which optimizes the Riemann solver to handle gravity terms and extends model applicability to three-dimensional reservoirs [20]. INSIM-FPT optimizes calculation accuracy for non-linear inter-well flow paths through virtual well refinement and path-tracking algorithms. At present, the INSIM series shows broad application prospects in history matching, production optimization, and macroscopic connectivity characterization of water-flooded reservoirs. Notably, to strengthen the seepage theoretical foundation of such methods, Zheng et al. further introduced generalized finite difference theory, constructed a non-Euclidean physically connected network equivalent model, and proposed the meshless Connection Element Method (CEM) [21]. The simplified treatment of inter-well connectivity in INSIM and the spatial discretization concept of CEM provide important theoretical support and inspiration for this study, regarding meshless streamline tracing and refined characterization of complex channeling pathways during profile control and flooding processes.

To date, numerical simulation techniques for chemical flooding have primarily evolved across three methodological paradigms, each exhibiting distinct computational and physical tradeoffs.

The first paradigm comprises conventional Grid-based Compositional Simulators formulated via finite volume or finite difference methods. These mechanistic models offer comprehensive descriptions of multiphase fluid flow coupled with intricate chemical phenomena, including multi-component mass transfer, competitive adsorption, and non-Newtonian fluid rheology [22, 23]. However, when applied to field-scale reservoirs with millions of grid blocks, they entail prohibitive computational overhead and suffer from severe grid-orientation effects, rendering real-time history matching and rapid optimization practically intractable.

To alleviate the computational burden, the second paradigm utilizes Streamline-based Simulators, which decouple the three-dimensional pressure field from the one-dimensional transport equations along dynamically updated streamlines [24, 25]. While streamline simulation drastically accelerates convective transport modeling and front tracking in large-scale heterogeneous formations, capturing complex physical-chemical interactions—such as shifting shear rates, variable adsorption-induced permeability reduction, and cross-streamline diffusion—remains highly challenging and computationally diffusive under transient flow conditions.

The third paradigm involves Reduced-Order Connectivity Models, such as

the Capacitance-Resistance Model (CRM) and early Inter-well Network Simulation Models (INSIM) [26]. By abstracting the continuous reservoir domain into a simplified discrete network of inter-well connections, these models eliminate the grid infrastructure entirely, enabling production performance forecasting and history matching to be executed orders of magnitude faster than conventional methods. Nevertheless, conventional connectivity formulations are fundamentally limited to waterflooding systems, as they typically treat fluid mobility as a constant or simplistic function, thereby failing to accommodate the strongly non-linear viscosity-thickening behaviors and rock-fluid interaction mechanisms inherent to polymer or profile-control agent transport.

Although meshless methods have achieved remarkable progress in reservoir connectivity characterization, existing studies mainly focus on water-flooded reservoirs. In this paper, the meshless Connection Element Method is extended to flow simulation of integrated profile control and flooding. The core novelty lies in dynamically coupling non-Newtonian polymer rheology and rock adsorption-induced permeability reduction directly into the meshless equations. To demonstrate the computational and physical tradeoffs of this approach relative to traditional paradigms, a comprehensive benchmarking is provided in **Table 1**. Under the meshless connection framework, a directed-graph depth-first search (DFS) algorithm is introduced to construct a complete topological structure containing injection wells, virtual connection elements, and production units, efficiently traversing complex tortuous flow trajectories deep in the reservoir. Meanwhile, two evaluation levels, element splitting and path splitting, are established to achieve full-scale quantitative characterization from microscopic node distribution to macroscopic pathway contribution, effectively solving difficulties in identifying hidden lateral channeling pathways. Instead of single-parameter evaluation, a weighted identification function is established by integrating flow distribution characteristics, channel conductivity, storage capacity, and overall heterogeneity. On this basis, a dimensionless channeling factor is defined to quantify how many times a single pathway exceeds the average conductivity of the entire reservoir. A four-level quantitative classification standard is established, including extreme channeling, strong channeling, weak channeling, and matrix seepage, promoting channeling evaluation from qualitative inference to spatial positioning and graded quantification. Based on accurate identification of preferential channeling pathways, coupled seepage and mass transfer mechanisms of chemical agent transport are incorporated into the meshless connection element model. It characterizes the non-Newtonian rheology of polymer agents and rock adsorption effects. Combined with classification results of channeling factors, targeted treatments are implemented. Topological blocking is applied to extreme channeling pathways, while deep profile control and flow field reconstruction are carried out for strong channeling pathways. This realizes deep integration of numerical simulation and reservoir engineering schemes, providing scientific decision support and technical guidance for stabilizing oil production and controlling water cut in mature oilfields. The core innovations of this study are explicitly summarized as follows: (1) The meshless Connection Element Method (CEM) is successfully extended to the integrated numerical simulation of chemical

profile control and flooding, coupling non-Newtonian polymer rheology and dynamic rock adsorption; (2) The flow-path tracking strategy originally in INSIM-FT is advanced to quantitatively characterize complex connectivity fields during chemical flooding; (3) A systematic quantitative evaluation index system is established, defining a dimensionless channeling factor to classify channeling paths into four levels, directly linking them to differentiated mitigation strategies.

Table 1. Comparison of various reservoir simulation methods for chemical flooding.

Simulation paradigm	Core advantages	Key limitations
Grid-based Simulators	Offers rigorous physical descriptions for complex multi-phase flow and chemical interactions.	Suffers from prohibitive computational overhead and severe grid-orientation effects for field-scale applications.
Streamline-based Simulators	Highly efficient for convective transport modeling and fluid front tracking.	Struggles with complex physical-chemical interactions and suffers from numerical diffusion during transient cross-flow.
Connectivity Models	Eliminates grid infrastructure to achieve extremely high computational efficiency for rapid history matching.	Traditionally limited to waterflooding, failing to accommodate non-linear polymer rheology and complex mass transfer.

2. Methodology

2.1. Governing equations of flow

In this study, the reservoir fluid is assumed to consist of oil and water phases. The two phases are immiscible, insoluble in each other, and free of chemical reactions. The fluids are considered incompressible, and the entire displacement process occurs under isothermal conditions. The porous medium is slightly compressible. This study neglects capillary and gravitational forces to simplify model derivation, which is reasonably applicable to high-velocity preferential channeling flow in mature oilfields where advective transport and horizontal pressure gradients dominate fluid flow.

Equations of motion for the oil and water phases:

$$\mathbf{v}_o = -\frac{\mathbf{K}k_{ro}}{\mu_o}\nabla p, \tag{1}$$

$$\mathbf{v}_w = -\frac{\mathbf{K}k_{rw}}{\mu_w}\nabla p. \tag{2}$$

Substituting the above equations of motion into the law of conservation of mass yields the continuity equations for oil and water:

$$\nabla \cdot (\rho_o \mathbf{v}_o) + q_o = \frac{\partial(\phi \rho_o S_o)}{\partial t}, \tag{3}$$

$$\nabla \cdot (\rho_w \mathbf{v}_w) + q_w = \frac{\partial(\phi \rho_w S_w)}{\partial t}. \tag{4}$$

And the saturation constraint equation must be satisfied:

$$S_o + S_w = 1. \tag{5}$$

In the above equations, the physical symbols are defined as follows: v_o, v_w is flow velocity vectors for the oil and water phases, m/s; K is the absolute permeability tensor of the reservoir rock, characterizing anisotropic features, m^2; k_{ro}, k_{rw} is the relative permeability of the oil and water phases, respectively, dimensionless. μ_o, μ_w

is dynamic viscosity of the oil and water phases, respectively, $Pa \cdot s$; ∇p is formation pressure gradient, Pa/m; q_o, q_w is source/sink term intensity for the oil and water phases per unit volume of rock, s^{-1}; ϕ is effective porosity of the rock, dimensionless; S_o, S_w is oil saturation and water saturation, respectively, dimensionless.

Polymer flooding represents a typical two-phase, multicomponent flow process involving oil and water. In this process, polymers, as active components, are dissolved in the aqueous phase. They improve the oil–water mobility ratio by increasing the viscosity of the water phase, thereby enhancing sweep efficiency. In this study, the viscosity and relative permeability of the oil phase are assumed to remain constant during displacement. Emphasis is placed on the nonlinear influence of polymer concentration variations on the rheological properties of the water phase. The viscosity of the polymer solution (aqueous phase) exhibits a nonlinear increasing relationship with polymer concentration. A cubic polynomial is adopted to modify this rheological behavior and characterize the viscosity-thickening effect.

$$\mu_p = \mu_w(1 + A_1 C_p + A_2 C_p^2 + A_3 C_p^3), \tag{6}$$

Where: μ_p is the viscosity of the polymer solution at the current concentration, $mPa \cdot s$; μ_w is the viscosity of pure water before the addition of polymer, $mPa \cdot s$; C_p is the mass concentration of polymer in the water phase, kg/m^3; A_1, A_2, A_3 is experimental fitting coefficients characterizing the law of viscosity change with concentration, dimensionless.

Equation (8) describes dissolved-polymer advection in the aqueous phase. Molecular diffusion/dispersion is neglected for the present channeling-dominated cases, but polymer retention is included in the total component balance through the solid-phase accumulation term introduced in Equation (14). This separation removes the earlier ambiguity between dissolved-phase transport and total polymer conservation. Reversible adsorption-desorption is represented by a kinetic Langmuir relation:

$$\frac{\partial C_{ad,i}}{\partial t} = k_a C_i \left(C_{max} - C_{ad,i}\right) - k_d C_{ad,i}. \tag{7}$$

Where $C_{ad,i}$ is the adsorbed polymer per unit rock mass at node i, C_i is the aqueous polymer concentration, C_{max} is the maximum adsorption capacity, and k_a and k_d are the adsorption and desorption rate constants, respectively. The fully implicit update of $C_{ad,i}$ is coupled to the aqueous accumulation and advective flux in Equation (14); the permeability reduction is updated from the retained polymer at every time step. These kinetic parameters must be calibrated against core-flood adsorption and pressure-drop data.

$$\frac{\partial(\phi S_w C_p)}{\partial t} + \frac{\partial(u_w C_p)}{\partial x} = 0. \tag{8}$$

Where: S_w is water saturation, dimensionless; u_w is Darcy flow velocity of the water phase, m/s.

To close the above system of equations, the initial states and boundary constraints of the physical model must be integrated. Initial conditions:

$$S_w(x, 0) = S_{wc}, C_p(x, 0) = 0. \tag{9}$$

Where, S_{wc} is irreducible water saturation, dimensionless.

Boundary conditions: The inlet end adopts boundary conditions (constant concentration injection), and the outlet end can adopt constant pressure boundary conditions depending on the situation.

$$\begin{cases} S_w(0,t) = 1 - S_{or} \\ C_p(0,t) = C_{p0} \end{cases}. \tag{10}$$

Where, S_{or} is residual oil saturation, dimensionless; C_{p0} is the initial concentration of polymer at the inlet, kg/m^3.

2.2. Meshless method discretization

The discretization process of the meshless method primarily involves the discretization implementation of mathematical theory, the geometric discretization of the computational domain, and the discrete representation of physical conservation equations. The core approach utilizes the GFD combined with the CEM to solve partial differential equations in reservoir numerical simulation.

2.2.1. Discretization of the computational domain

The Generalized Finite Difference Method (GFDM) is a highly flexible strong-form meshless collocation method [27]. Unlike conventional grid-based methods, it does not rely on nodal topological structures. Its core principle is based on local Taylor series expansion and the Moving Least Squares (MLS) approximation theory. All spatial partial derivatives of unknown physical variables (such as pressure and saturation) are approximated as linear combinations of functional values at nodes within the local support domain. This method directly solves partial differential equations using a point cloud structure and is particularly suitable for problems with complex geometric boundaries. In discretizing the computational domain, random or regular nodes are first distributed over the entire region, including boundaries. To perform local approximation, a local interaction region, namely the support domain, is defined for any selected central node M_0 in the domain. During discretization, taking an arbitrary central node M_0 as the center, N neighboring nodes are selected within a specified radius r_s according to the shortest-distance criterion to form the local support domain. As shown in **Figure 1**, the distributed nodes are marked as black dots, the nodal support domains are represented by red dashed circles, and the connecting elements between nodes are shown as green lines. A larger support domain increases the number of connecting elements, thereby enriching the overall flow connection paths.

Detailed sensitivity analysis of the support domain radius r_s within the Generalized Finite Difference Method (GFDM) framework has been extensively discussed in the existing literature [28]. To ensure high computational accuracy while maintaining the solvability of the unknown function's spatial derivatives, a relatively small support radius is preferred. Consequently, the connection topology adopted in this study utilizes a Delaunay-like triangulation network to guarantee local approximation precision.

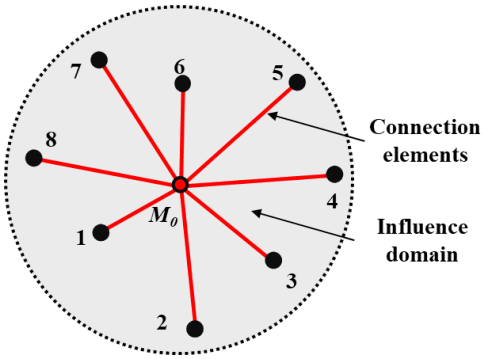

Figure 1. Construction of connection elements in the discretization of the computational domain.

2.2.2. Equation discretization

First, for any central node within the computational domain, the mass conservation law is applied to its control volume. The previously established continuity equations for oil and water two phases are volume-integrated over the control domain [29]. According to the mean value theorem for integrals, the rock and fluid physical parameters are assumed to be uniformly distributed within the control domain. Accordingly, the convective terms (divergence terms) on the left-hand side of the equation can be converted into volume-averaged expressions.

$$\int_{V_i} \nabla \cdot (\lambda \nabla p) dV + \int_{V_i} q dV = \int_{V_i} C_t \phi \frac{\partial p}{\partial t} dV. \tag{11}$$

Where, $\lambda = Kk_r/\mu$ represents the fluid mobility.

To solve the pressure diffusion term, the GFDM based on Taylor expansion and the weighted least squares principle is introduced. This method utilizes neighboring nodes to construct a meshless approximation, representing the 2D Laplace operator as a weighted linear combination of pressure differences between adjacent nodes.

$$\Delta p(M_0) = \frac{\partial^2 p}{\partial x^2} + \frac{\partial^2 p}{\partial y^2} = \sum_{m=3}^{4} \sum_{j=1}^{n} e_{ng}^{i,j} (p_j - p_i). \tag{12}$$

Where, M_0: is the spatial position coordinates of the central node i; $e_{ng}^{i,j}$: is the generalized finite difference geometric coefficient derived from GFD, which depends solely on the topological structure of the point cloud and is dimensionless.

Substituting Equation (12) into Integral Equation (11), and after rearrangement, the connection transmissibility is defined as a lumped parameter coupling the differential operator and reservoir physical properties:

$$T_{ij} = \beta \cdot V_i \cdot \lambda_{ij} e_{ng}^{i,j}. \tag{13}$$

Where, λ_{ij} is the harmonic average mobility between node i and j; β is the unit conversion coefficient.

It should be pointed out that the detailed calculation and rigorous derivation of the seepage characteristic parameters based on the meshless connection system have been systematically elaborated in existing literature [30]. Building upon this foundational

framework, the core contribution of this study is the successful extension of this method to the numerical simulation of complex chemical flooding. Furthermore, we leverage the distinct advantages of the meshless topological structure by introducing a directed-graph path-tracking algorithm to efficiently identify and precisely characterize complex fluid channeling pathways.

Based on the control volume conservation principle of the meshless CEM, and considering advective transport within the fluid phase, adsorption-retention on the porous media surface, and source/sink effects, a fully implicit discretized mass conservation equation for chemical components is constructed. For any central node$i$ within a time step Δt, its discretized governing equation is expressed as follows:

$$\begin{aligned}&\frac{V_{p,i}}{\Delta t}(S_{w,i}^{n+1}C_i^{n+1}-S_{w,i}^{n}C_i^{n})+\rho_r V_{s,i}\frac{C_{ad,i}^{n+1}-C_{ad,i}^{n}}{\Delta t}=\\&\sum_{j\in\Omega_i}(q_{ij}^{n+1}\cdot C_{ij}^{up})+Q_{inj,i}C_{inj}-Q_{prod,i}C_i^{n+1}\end{aligned}\tag{14}$$

Where, $V_{p,i}$ is effective pore volume, m^3; $V_{s,i}$ is rock matrix volume, m^3; ρ_r is rock matrix density, kg/m^3; $S_{w,i}$ is water saturation, dimensionless; C_i is chemical agent concentration in the water phase at node i, kg/m^3; $C_{ad,i}$ is adsorption amount of the chemical agent per unit mass of rock at node i, kg/kg; q_{ij} is volumetric flow rate of the water phase between node i and its neighboring node j, m^3/d; C_{ij}^{up} is upstream concentration at node i, m^3/d; $Q_{prod,i}$: Injection rate at node i, m^3/d.

2.3. Quantitative characterization of dynamic reservoir connectivity

To overcome the limitations of traditional grid-based numerical simulation systems in intuitively capturing inter-well flow interactions (such as the identification of water channeling paths), the meshless CEM is introduced. Under the meshless CEM framework, a multi-dimensional and multi-scale connectivity index evaluation system has been established. This system integrates core indicators, including split coefficients, connection transmissibility, connection volume, and the Lorentz coefficient. It aims to provide a comprehensive and quantitative characterization of complex dynamic reservoir connectivity, ranging from microscopic nodal interaction mechanisms to macroscopic reservoir heterogeneity features.

2.3.1. Quantitative analysis of dynamic connectivity

Under the computational framework of the meshless CEM, fluid transport between injection and production wells is not a simple point-to-point linear flow. Instead, it is based on a complex topological network where multi-level diversion and redirection occur through multiple “virtual nodes” (intermediate connection elements or indirect connection points). To overcome the limitations of traditional grid-based methods in describing these implicit flow interactions, a path-tracking algorithm is introduced. A two-level split coefficient evaluation system, ranging from microscopic elements to macroscopic paths, has been constructed to achieve precise quantification of flow allocation. The unit split coefficient is the core index characterizing the primary distribution of fluid by the local connectivity structure. Physically, it is defined as the ratio of the liquid flux flowing from a specific connection node i toward a specific

downstream adjacent node j under a pressure-driven gradient, relative to the total liquid outflow from node i. Its calculation formula is as follows:

$$\varphi_{i,j}^{n} = \frac{q_{i,j}^{n}}{\sum_{k=1}^{n_c} q_{k,j}^{n}} \tag{15}$$

Where, $q_{i,j}^{n}$ represents the flow rate from node i to node j; $\sum_{k=1}^{n_c} q_{k,j}^{n}$ represents the total outflow from node j.

To address the numerous indirect connection relationships (virtual wells) between injection and production wells, this study introduces the directed graph-based Depth-First Search (DFS) algorithm [31]. This algorithm recursively traverses complex nodal connection relationships to efficiently track all potential connectivity trajectories and eliminate redundant calculations or cyclic iteration problems. In this study, the path split coefficient is defined as the cumulative product of the unit split coefficients of all connecting elements that constitute the flow path k. The corresponding mathematical expression is presented as follows,

$$\varphi_{2,1}^{n,k} = \varphi_{3,1}^{n} \times \varphi_{2,3}^{n}. \tag{16}$$

Figure 2 illustrates the connectivity relationships within the study area. In this diagram, circular symbols represent different types of well points: white denotes injection wells, red denotes production wells, and black denotes virtual wells. These well points are interconnected by line segments, with each segment corresponding to a specific connection element. Notably, each connection element is marked with an arrow, which clearly indicates the direction of fluid flow, providing an intuitive reference for analyzing injection-production relationships.

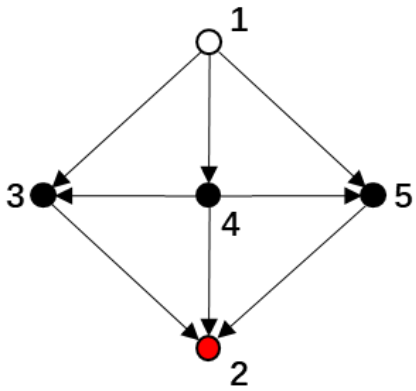

Figure 2. Schematic diagram of the model.

The path split coefficient is generalized to any arbitrary path, and the formula is expressed as:

$$\varphi_{path}^{k} = \prod_{(i,j)\in Path_k} \varphi_{i,j}^{n}. \tag{17}$$

This index directly reflects the hydraulic contribution of the path. If the φ_{path}^{k} of a specific path is significantly higher than that of other paths, it is identified as a preferential channeling path.

Algorithmic Workflow for DFS-Based Path Identification: To ensure computational reproducibility, the extraction of inter-well flow paths is executed through the following procedure:

1. Graph construction: The reservoir domain is initialized as a directed graph, where injection wells, virtual connection elements, and production wells represent the nodes. The connection elements, carrying specific unit split coefficients ($\varphi_{i,j}^{n}$), serve as the directed edges mapping the fluid flow direction.
2. Traversal strategy: A recursive Depth-First Search (DFS) algorithm is initiated from each active injection node. The algorithm explores as far as possible along each branch before backtracking, logging the unit split coefficients of every visited edge.
3. Termination criteria: The recursive search for a specific branch terminates when the traversal successfully reaches a production well node (valid path) or encounters a dead-end boundary node with zero outflow (invalid path). Cyclic loops are prevented by flagging visited nodes.
4. Path evaluation and ranking: For every valid path k connecting an injector to a producer, the macroscopic path split coefficient (λ_{path}^{k}) is calculated as the continuous product of its constituent unit split coefficients. All tracked paths are then ranked in descending order based on their (λ_{path}^{k}) values to identify the dominant fluid trajectories carrying the highest volumetric allocation.

Unlike the split coefficient, which emphasizes flow distribution proportions, the inter-well transmissibility and connection volume focus on the physical properties of the connection units themselves. Connection transmissibility is a dynamic parameter describing the fluid exchange capacity between nodes, comprehensively reflecting the influence of reservoir permeability, the size of the nodal control volume, and topological connection relationships. Numerically, it determines the flow rate through the connection unit under a unit pressure difference. Within the meshless framework, the control volume of each node V_i must first be determined. Based on generalized difference operators and local conservation of mass, the following system of equations is established:

$$\begin{cases} V_i \sum_{m=3}^{4} e_{mj}^{i} = V_j \sum_{m=3}^{4} e_{mi}^{j} \\ \sum_{i} V_i = V_R \end{cases}. \tag{18}$$

Where, e_{mj}^{i} represents the geometric coefficient in the difference scheme, V_R is the total reservoir volume. By solving this system of equations simultaneously, the control volume V_i for each node is obtained.

In the derivation of the meshless connectivity system, the specific calculation formula for connection transmissibility is,

$$T_{ij} = \lambda_{ij} k_{ij} V_i \sum_{m=3}^{4} e_{mi}^{j} = \lambda_{ji} k_{ji} V_j \sum_{m=3}^{4} e_{mj}^{i}. \tag{19}$$

Connection volume is a unique geometric attribute parameter in the CEM, serving the physical purpose of quantitatively characterizing the effective space of a connection element for fluid storage and transport. As a geometric invariant of the connection

element, its value is determined solely by the spatial distribution and topological structure of the initial nodes, independent of reservoir physical properties such as permeability and porosity. To ensure the macroscopic material balance of the physical model, the sum of the volumes of all connection elements across the entire domain must be strictly constrained by the total reservoir volume. The physical conservation formula is as follows:

$$\sum_{k=1}^{N_{conn}} V_{conn,k} = V_{total}. \tag{20}$$

Where, N_{conn} is the total number of connection elements, V_{total} is the total volume of the reservoir computational domain.

As is well known, in the traditional grid-based reservoir numerical simulation (FVM), the conductivity coefficient is defined as follows:

$$T'_{ij} = \lambda_{ij}\frac{k_{ij}A_{ij}}{L_{ij}} = \lambda_{ij}\frac{k_{ij}A_{ij}d_{ij}}{L_{ij}^2} = \lambda_{ij}\frac{k_{ij}V'_{ij}}{L_{ij}^2}. \tag{21}$$

Among them, A_{ij} represents the cross-sectional area of two adjacent grids; L_{ij} represents the distance between the centers of the two grids. V'_{ij} represents the connection volume between grid i and grid j. Therefore, there exists the following proportional relationship between the conduction coefficient and the connection volume:

$$\frac{T'_{ij}L_{ij}^2}{\lambda_{ij}k_{ij}} \propto V'_{\ddot{v}}. \tag{22}$$

Similarly, when deriving the calculation formula for the connection volume, it is also assumed that there exists the following relationship between the conductivity and the connection volume:

$$\frac{T_{ij}L_{ij}^2}{\lambda_{ij}k_{ij}} \propto V_{ij}. \tag{23}$$

By combining the proportional relationship with the conservation constraint, the explicit expression for the connection volume V_{ij} is obtained:

$$V_{ij} = \frac{\frac{T_{ij}L_{ij}^2}{\lambda_{ij}k_{ij}}}{\sum_{i=1}^{N-1}\sum_{i<j}^{N}\frac{T_{ij}L_{ij}^2}{\lambda_{ij}k_{ij}}}V_R. \tag{24}$$

Where, V_{ij} is the connection volume; T_{ij} is the connection transmissibility; L_{ij} is the node spacing; k_{ij} is the average permeability of the connection element; λ_{ij} is the mobility or proportional coefficient; V_R is the total reservoir volume.

This mapping mechanism ensures that the adjustment of connection element parameters in numerical simulation can be inversely reflected in the physical parameters of nodal control regions, thereby realizing high-precision inversion of reservoir heterogeneity. As a core weighting parameter, the connected volume not only quantifies the fluid retention space within the topological network but also governs the propagation speed of chemical agents and fluid fronts along different pathways, making it a key physical quantity for identifying preferential channeling routes. Within the meshless connection element model, the construction of the Lorenz curve depends on

two essential parameters: the inter-well conductivity T_{ij} reflecting seepage velocity and the inter-well connection volume V_{conn} characterizing material accumulation capacity. The specific implementation proceeds as follows: first, define the flow velocity index V_k of each connection element; according to Darcy's law, flow velocity is proportional to conductivity and inversely proportional to connected volume. All effective flow pathways in the domain are sorted in descending order by this index, so that potential channeling paths with high conductivity and small volume can be preferentially identified. Based on the sorted sequence of connection elements, two dimensionless cumulative distribution functions are calculated. Among them, the cumulative flow capacity (F_k) represents the proportion of the total conductivity contributed by the first k connection elements, characterizing the dynamic flow contribution, and its computational formula is given as follows.

$$F_k = \frac{\sum_{i=1}^{k} T_i}{\sum_{j=1}^{N_{conn}} T_j}. \tag{25}$$

Where, F_k is cumulative flow capacity; T_i/T_j is connection transmissibility.

Cumulative Storage Capacity (C_k) represents the cumulative share of the total connection volume of the first k connection elements relative to the field-wide total connection volume after sorting, characterizing the static contribution of the reservoir space. Its calculation formula is:

$$C_k = \frac{\sum_{i=1}^{k} V_{conn,i}}{\sum_{j=1}^{N_{conn}} V_{conn,j}}. \tag{26}$$

Where, N_{conn} is the total number of connection elements. The curve plotted with C_k as the abscissa and F_k as the ordinate is the dynamic connectivity Lorentz curve for the reservoir model.

To convert the characteristics of the curve into a quantitative evaluation index, the Lorentz coefficient (L_c) is defined as twice the area enclosed between the Lorentz curve and the line of absolute homogeneity (i.e., the diagonal). Its mathematical expression is:

$$L_c = 2\left(\int_0^1 F(C)dC - 0.5\right). \tag{27}$$

Where, $\int_0^1 F(C)dC$ is the area enclosed by the Lorentz curve and the coordinate axes. The Lorentz coefficient intuitively reflects the degree of mismatch between internal flow capacity and storage capacity within the reservoir. It serves as a critical basis for identifying preferential inter-well flow channels and diagnosing ineffective water circulation.

2.3.2. Flow path characterization

Flow paths refer to the primary flow channels selected by fluids during transport within a reservoir under the influence of reservoir heterogeneity. These paths possess physical characteristics such as low flow resistance and high conductivity. In the connectivity index system established in this study, a flow path is defined as one or more connectivity trajectories with the maximum path split coefficient (λ_{path}).

Specifically, among the multiple potential connectivity paths existing between injection and production wells, the flow path is the trajectory that carries the vast majority of the injected fluid volume allocation. In numerical terms, a threshold is typically given based on field requirements, or the top paths with the largest injection-production split values are directly selected as flow paths. The maximum split coefficient between two wells, $\Psi_{i,j}^{n}$ is defined as the maximum of all path split values:

$$\Psi_{i,j}^{n} = \mathrm{MAX}(\varphi_{i,j}^{n,p}). \tag{28}$$

To extract the flow field skeleton from complex background streamlines, this study formulates a quantitative screening criterion based on split coefficients: all effective paths between a specific injection-production well pair are ranked in descending order according to the path split coefficient λ_{path}. Screening conditions are then established based on field development requirements. For example, one can select the top n paths with the largest split coefficients or retain paths with split coefficients greater than a specified threshold. The screened paths with high split values are defined as preferential flow paths. In this study, the two paths with the largest split values for each injection-production well pair are selected as the flow paths, and the red lines represent the inter-well flow path results. In visual characterization (as shown in **Figure 3**), these paths are typically marked with prominent colors (such as bold red lines) to intuitively outline the primary breakthrough directions of the fluid in the deep reservoir.

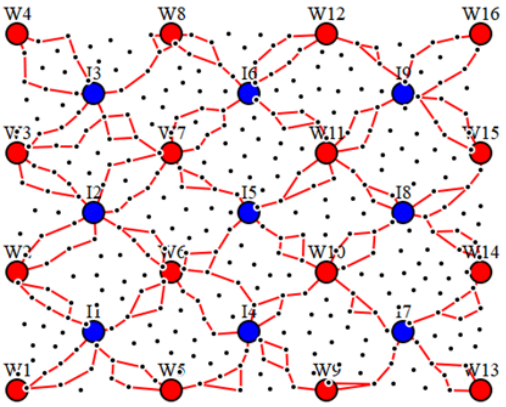

Figure 3. Screened flow paths [32].

2.3.3. Identification and mitigation of channeling paths

To accurately identify preferential channeling paths from a vast number of potential connectivity trajectories, this study constructs a multi-parameter coupled weighted identification function for channeling, W_k. This function comprehensively considers the flow allocation of the path (split coefficient λ), flow capacity (transmissibility T), storage space (connection volume V), and field-wide heterogeneity (Lorentz coefficient L_c). The weighted identification index W_k for the k path is defined as follows:

$$W_k = \underbrace{(1+L_c)^{\alpha}}_{\text{Heterogeneity gain term}} \cdot \underbrace{\lambda_{path}^{k}}_{\text{Flow contribution term}} \cdot \underbrace{\left(\frac{T_{path}^{k}}{V_{path}^{k}}\right)}_{\text{Velocity characteristic term}}. \tag{29}$$

Where, λ_{path}^{k} characterizes the proportion of injected water allocation carried by the path. A higher value indicates a higher risk of channeling. $\bar{T}_{path}^{k}/\bar{V}_{path}^{k}$ is the ratio of the average path connection transmissibility to the average connection volume. Physically, it is directly proportional to the actual advancement velocity of the fluid in the pores. Higher transmissibility and smaller volume result in faster flow velocity and earlier breakthrough. L_c (Lorentz coefficient): The field-wide connectivity heterogeneity coefficient ($0 \leq L_c \leq 1$). This parameter is introduced as a global sensitivity factor. When the reservoir heterogeneity is extremely strong ($L_c \to 1$), the amplification effect of the function on high-velocity paths significantly enhances, thereby capturing preferential channels more acutely. α: An adjustment factor used to control the degree of influence of heterogeneity on the identification weight. W_{th} The identification threshold. When $W_k > W_{th}$, path k is determined to be a preferential channeling path.

Calibration of the heterogeneity weight α: α controls how strongly the Lorenz coefficient amplifies the path-scale velocity indicator. We use $\alpha = 1$ as the neutral baseline and recommend screening $0 \leq \alpha \leq 2$ against tracer-labelled or production-diagnosed channels. For each candidate α, the classification threshold is recalibrated on the training period and assessed on a held-out period using precision, recall, F1 score, and water-breakthrough timing error. The selected α is the smallest value within one standard error of the best validation score, limiting over-amplification.

After determining the scope of channeling paths through the weighted function, this paper defines a new dimensionless evaluation index—the channeling factor (η)—to further quantify the urgency of treating individual channels. This factor normalizes the calculation results of the weighted function, intuitively reflecting the "advantage multiple" of a specific path relative to the field average level. Its calculation formula is as follows:

$$\eta_k = \frac{W_k}{\frac{1}{N}\sum_{i=1}^{N} W_i} = \frac{\lambda_{path}^{k} \cdot (T_k/V_k)}{\langle \lambda \cdot T/V \rangle_{avg}}. \tag{30}$$

Where: W_k: is the weighted identification index of the path; N: is the total number of effective paths; λ_{path}^{k}: is the path split coefficient; T_k: is the average path connection transmissibility; V_k: is the average path connection volume; T_k/V_k: is the velocity characteristic ratio; $\langle \lambda \cdot T/V \rangle_{avg}$: is the field-wide average characteristic value.

The channeling factor thresholds in **Table 2** were empirically calibrated using production and tracer data from the target field, achieving a 70%–80% accuracy in identifying preferential pathways. While providing a practical baseline for mature sandstone reservoirs, these parameters are phenomenological rather than universally applicable. Dynamic recalibration based on local historical data is required when extending this framework to reservoirs with distinct geological settings.

Table 2. Classification of preferential channels based on the channeling factor.

Channeling factor range	Channeling grade	Corresponding geological characteristics
$\eta_k > 0.8$	Level-I Channeling (Extreme)	Large-scale fractures or vuggy channels
$0.5 < \eta_k \leq 0.8$	Level-II Channeling (Strong)	High-permeability streaks
$0.2 < \eta_k \leq 0.5$	Level-III Channeling (Weak)	General preferential flow channels
$\eta_k \leq 0.2$	Matrix flow	Normal displacement zones

3. Numerical experiments

3.1. Conceptual case

A three-layer heterogeneous reservoir model was established, with each layer containing a varying number of high-permeability streaks. The flow field distribution of the permeability for each layer is shown in **Figure 4**.

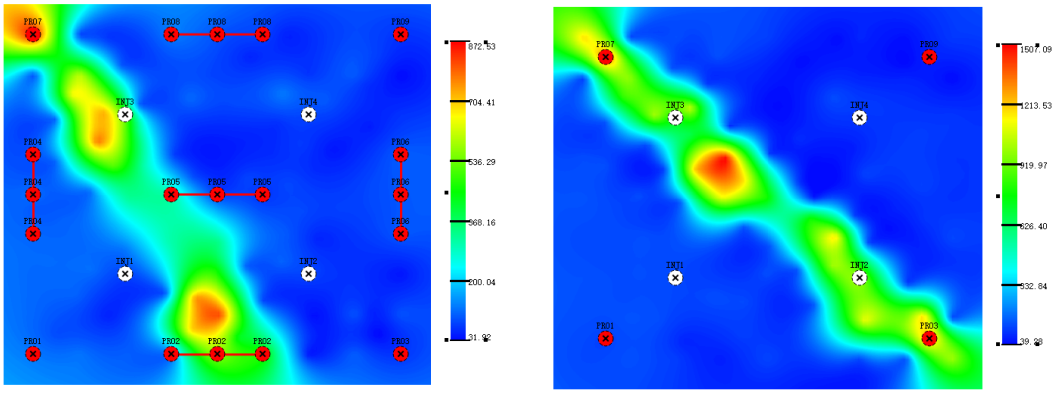

(a) Layer 1 **(b)** Layers 2 and 3

Figure 4. Permeability field distribution (logarithmic scale).

The reservoir model consists of 25 × 25 × 3 grids in the X, Y, and Z directions, with grid dimensions of 40 m, 40 m, and 10 m, respectively. The average permeability of each reservoir layer is 178.24 mD and 319 mD. The irreducible water saturation is 0.8, and the porosity is 0.2 for all layers. Other physical parameters are listed in **Table 3**. A five-spot well pattern is utilized, with a total of 13 wells deployed, including 9 production wells and 4 injection wells.

Table 3. Selected physical parameters of the reservoir model.

Parameter	Value
Initial reservoir pressure (MPa)	25
Rock compressibility (MPa^{-1})	1.45×10^{-4}
Oil phase compressibility (MPa^{-1})	5.00×10^{-5}
Water phase compressibility (MPa^{-1})	5.00×10^{-5}
Oil phase viscosity (mPa·s)	10.0
Water phase viscosity (mPa·s)	1.0

Since the injection well INJ3 is located on high-permeability streaks in all three reservoir layers, and INJ2 is situated on a high-permeability streak in the first layer, long-term water injection in INJ2 and INJ3 will lead to the formation of preferential flow paths along these streaks. Consequently, injected water will flow preferentially along these channels, resulting in low displacement efficiency and lower water injection efficiency compared to wells INJ1 and INJ4. Therefore, these wells can be selected as candidates for profile control.

Considering the near-wellbore effects, as shown in **Figure 5**, the nodal density around injection wells INJ2 and INJ3 was increased during the construction of the CEM simulation model to ensure more refined local connectivity. The resulting connection transmissibility and connection volume for the model are illustrated in **Figure 6**.

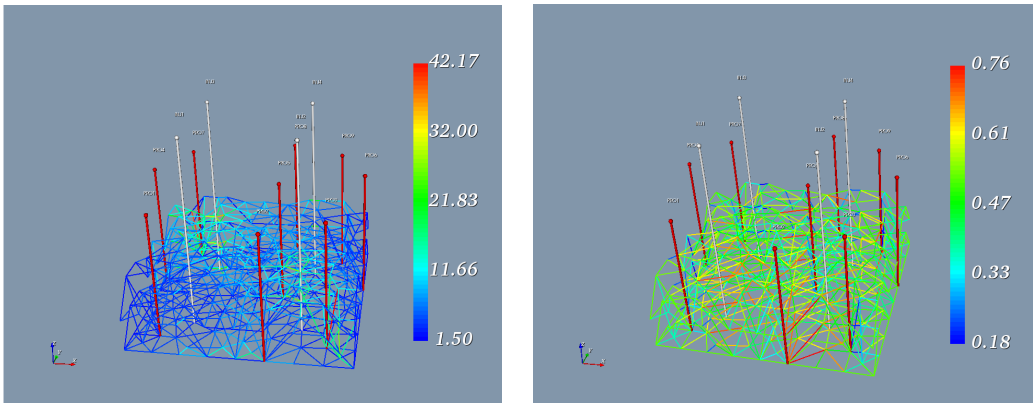

(a) Connection transmissibility **(b)** Connection volume

Figure 5. 3D Connectivity Diagram of the CEM Simulation Model.

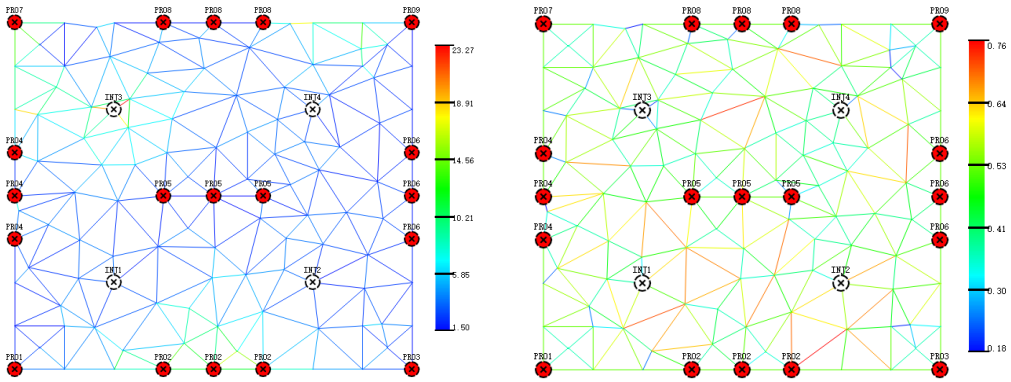

(a) Connection transmissibility **(b)** Connection volume

Figure 6. 2D Connectivity Diagram of the CEM Simulation Model.

Initially, a water-flooding production period of 2,100 days was set, consisting of 70 time steps with a step length of 30 days/step. The injection wells were controlled by a fixed injection rate of 225 m^3/d, while production wells were controlled by a fixed liquid production rate of 100 m^3/d. The calculated results for the production water cut are shown in **Figure 7**.

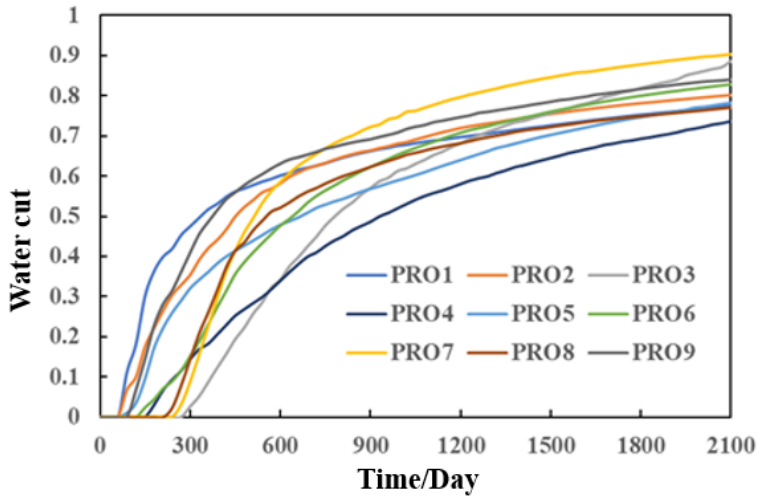

Figure 7. Calculated results of production well water cut.

Figure 7 illustrates the calculated water cut results for the production wells after 2,100 days of production. It is observed that the water cut for all nine production wells has exceeded 80%. Specifically, the water cut for production well PRO7, which is situated on high-permeability streaks across two reservoir layers, has surpassed 90%. Given that the water cut of the production wells is generally at a high level, it indicates that stable flow paths have formed within the reservoir, leading to severe ineffective circulation of injected water. To address this, based on the previously established quantitative identification method for channeling paths, an inversion of the connectivity status between all injection and production wells was performed to calculate the streamline split coefficients and the periodic water injection efficiency for each injection well. Through a coupled analysis of the spatial distribution of preferential channels and the utilization efficiency of injection wells, the primary injection directions controlling low-efficiency and ineffective circulation were precisely localized. According to the calculation results, the injection well with the lowest water injection efficiency was selected as the target for deep profile control operations. The objective is to plug the high-conductivity streaks and force the subsequently injected fluids to undergo flow redirection, thereby expanding the sweep volume and improving development performance.

Figure 8 illustrates the calculated water injection efficiency of all injection wells. Among them, Well INJ2 shows the poorest performance and is thereby determined as the optimal candidate for profile control treatment. This well is selected to characterize reservoir production dynamics after plugging agent injection, with the agent injection volume specified as 8,000 m. Numerical simulations are carried out under the defined parameters to investigate the production responses after the implementation of Integrated Profile Control (IPC) measures, and the corresponding results are displayed in **Figure 9**. **Figure 9a** presents the correlation between the volume expansion factor and the conductivity decline coefficient. The concentration curve increases sharply to a peak before declining steadily, which verifies that the injected chemical agent efficiently migrates toward production well regions. **Figure 9b** compares the temporal variation of water cut before and after treatment. To quantitatively validate the reliability of the developed model, the simulation results are cross-checked with outputs from the commercial CMG simulator. The water cut curve predicted by the proposed model (blue line) achieves excellent consistency with the CMG results (green line), with a highly accurate RMSE of only 3.8%. Compared with the untreated baseline case, a remarkable decrease in water cut is achieved after IPC treatment. This outcome demonstrates that plugging the high-permeability channels surrounding Well INJ2 effectively reroutes the injected water stream, restrains the uncontrolled rise in water cut, and realizes a favorable water control effect.

To quantitatively evaluate the accuracy and computational efficiency of the proposed CEM framework, a comprehensive benchmarking analysis was conducted against the standard commercial grid-based simulator. The key validation metrics, including the water cut root-mean-square error (RMSE), execution runtimes, and model discretization scales, are consolidated in **Table 4**. The comparative data demonstrate that the meshless connection network yields a highly consistent match

with the commercial simulator, maintaining the water cut RMSE well within acceptable engineering tolerances. Crucially, by reducing the structural degrees of freedom from thousands of grid blocks to a streamlined nodal network, the proposed model achieves a drastic reduction in computational cost. This significant acceleration firmly confirms the viability of the CEM framework for rapid field-scale history matching and performance forecasting.

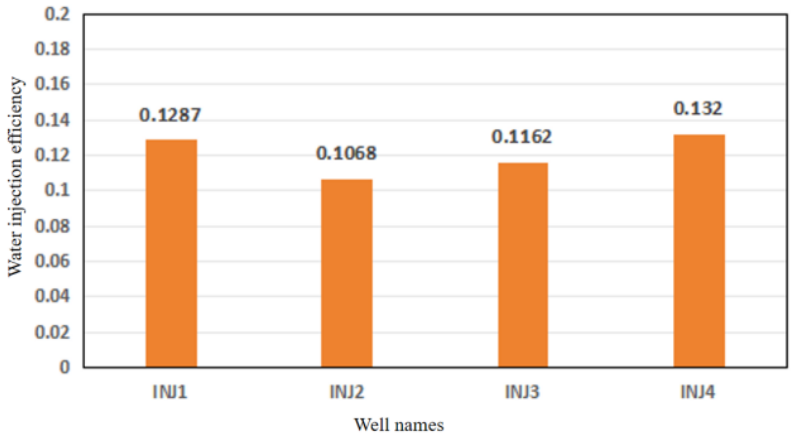

Figure 8. Calculation results of water injection efficiency for injection wells.

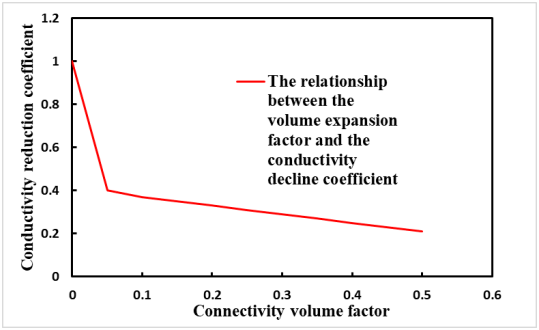

(a) The relationship between the volume expansion factor and the conductivity decline coefficient

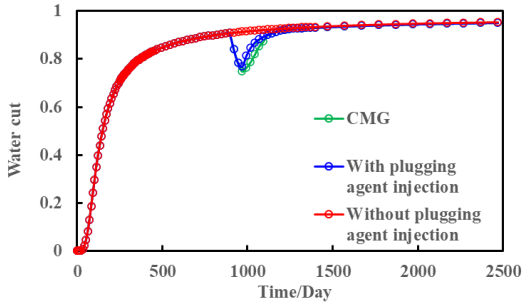

(b) Water cut

Figure 9. Production performance curves.

Table 4. Quantitative validation of the proposed CEM model vs. a commercial simulator.

Parameter	CEM model	Commercial simulator
Water Cut RMSE (%)	3.8%	Benchmark
Computational Time (s)	1.6 s	7.3 s
Model Discretization (Grids/Nodes)	5 Nodes	2,500 Grid Blocks

To further reveal the physical mechanism of chemical agents in improving development performance from the perspective of microscopic flow fields, the established meshless CEM model was utilized to calculate and compare the distribution changes of streamline split coefficients for injection wells in each layer before and after the implementation of profile control measures. Comparing **Figure 10**, it can be intuitively observed that prior to profile control, the split coefficients of injection wells in the direction of preferential channels were relatively high, indicating that the injected water primarily broke through along high-permeability zones. Following the

implementation of deep profile control, the split coefficients in the direction of the preferential channels decreased significantly, and the color representing the originally strong channeling direction transitioned from deep red to a lighter shade or decreased in numerical value. Meanwhile, the split coefficients in the lateral non-preferential directions increased, demonstrating that the chemical agents effectively plugged the high-conductivity channels and forced the injected fluid to redirect. This subsequently swept into the low-permeability regions with originally low displacement degrees, achieving an effective displacement of the water injection profile.

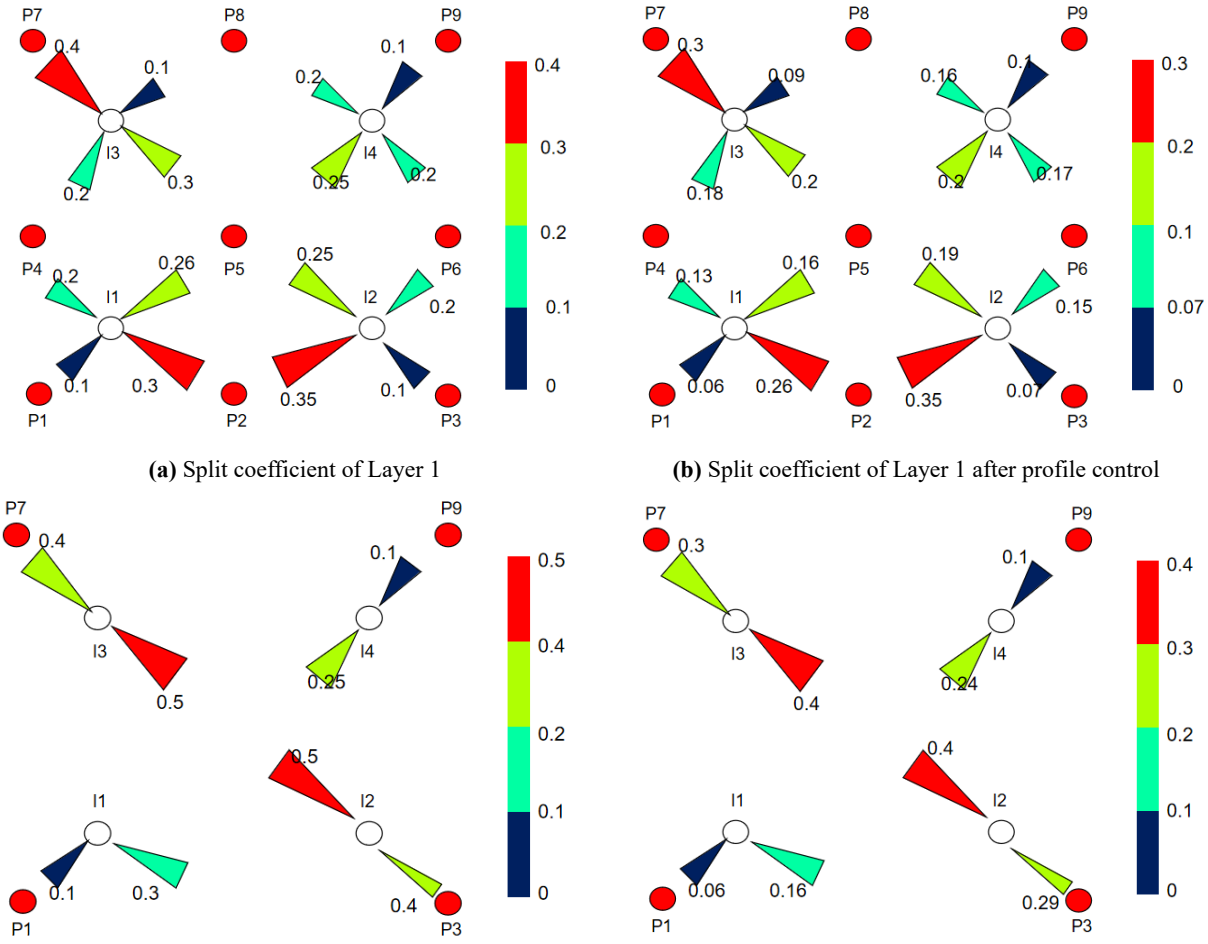

(a) Split coefficient of Layer 1

(b) Split coefficient of Layer 1 after profile control

(c) Split coefficient of Layer 2

(d) Split coefficient of Layer 2 after profile control

Figure 10. Changes in split coefficients before and after profile control.

To further intuitively reveal the spatial distribution morphology of the preferential channels, representative injection-production well groups I3-P7 and I2-P3 were selected for visual analysis of their primary inter-well flow paths, as shown in **Figure 11**. It can be observed that when injection well I3 supplies water to production well P7, the process is primarily controlled by Flow Path 1 and Flow Path 2. Both paths are strong channeling channels with high conductivity, leading to the rapid short-circuiting of injected water along these directions and resulting in extremely low sweep efficiency. In the I2-P3 well group, Flow Path 3 exhibits significant Level-I preferential channel characteristics, carrying the vast majority of the injected fluid volume and establishing a dominant position in that direction. In contrast, Flow Path 4 is represented by a lighter color, indicating a matrix flow region with higher flow resistance. This extreme

heterogeneity of flow paths provides a precise spatial localization basis for subsequent targeted profile control.

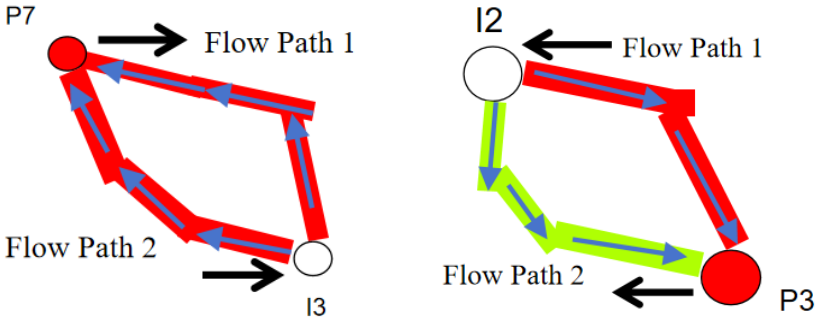

(a) Split coefficient of Layer 1 **(b)** Split coefficient of Layer 1 after profile control

Figure 11. Flow paths.

Figure 12 illustrates the changes in connection transmissibility before and after profile control. The color and thickness of the connection elements represent the magnitude of the connection transmissibility; a larger transmissibility is indicated by a thicker line. It can be observed that after the injection of the plugging agent, the connection transmissibility of the connection elements surrounding the injection well INJ2 decreases to varying degrees, reflecting the effective plugging of the formation following the injection.

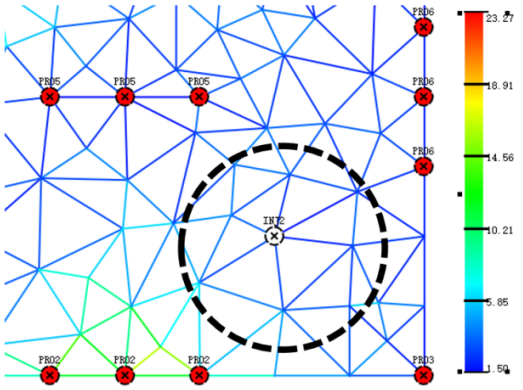

(a) Connection transmissibility of Layer 1 (Before profile control)

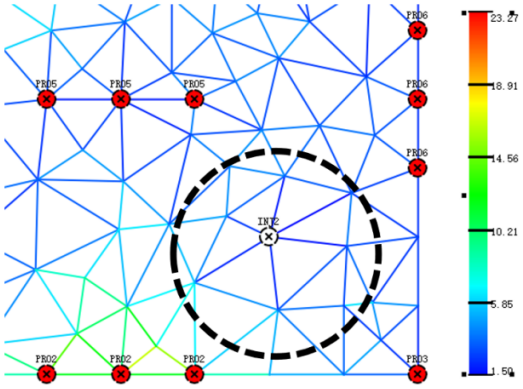

(b) Connection transmissibility of Layer 1 (After profile control)

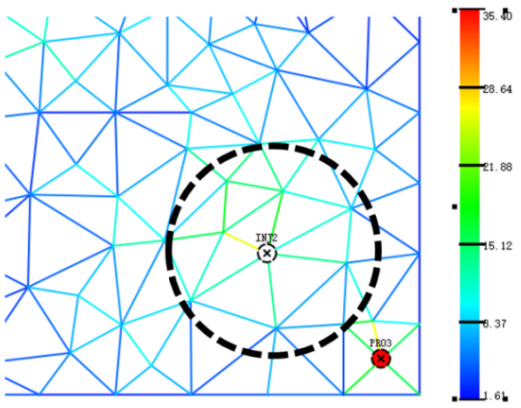

(c) Connection transmissibility of Layer 2 (Before profile control)

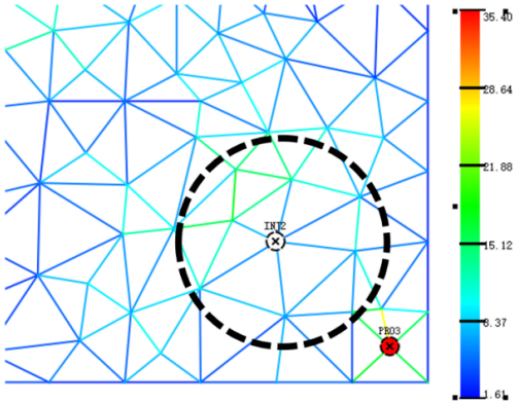

(d) Connection transmissibility of Layer 2 (After profile control)

Figure 12. *Cont.*

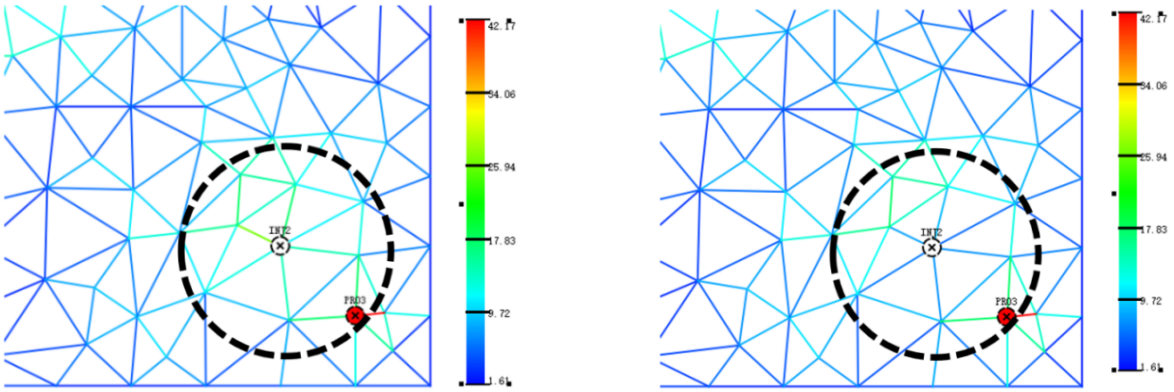

(e) Connection transmissibility of Layer 3 (Before profile control) **(f)** Connection transmissibility of Layer 3 (After profile control)

Figure 12. Changes in connection transmissibility before and after profile control.

Figure 13 shows the production dynamic prediction results of the well group after the injection of the plugging agent. It can be seen that, compared to the scenario without plugging agent injection, the daily oil production of the well group increases and the water cut decreases within approximately 1,000 days after injection, achieving the effect of reducing water and increasing oil. However, after 1,900 days, the plugging effect of the agent gradually diminishes, and the daily oil production of the well group no longer increases.

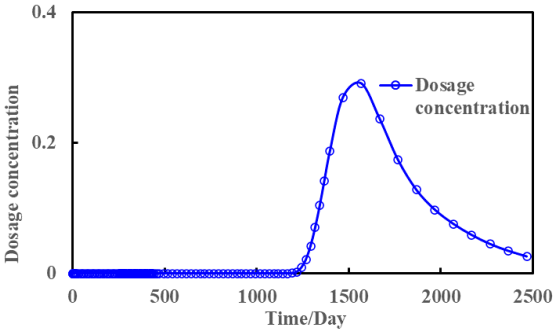

(a) Dosage concentration

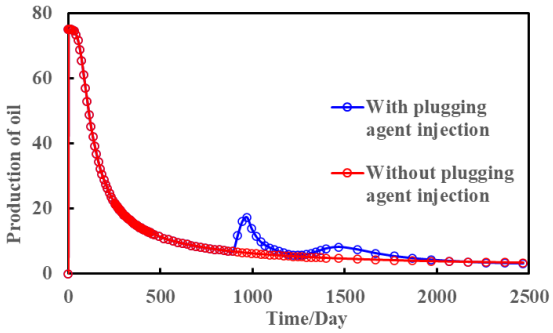

(b) Prediction results of daily oil production after plugging and profile control

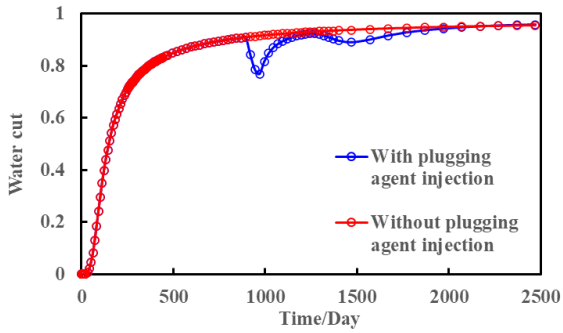

(c) Prediction results of water cut after plugging and profile control

Figure 13. Dynamic prediction results of the well group after implementing profile control in injection well INJ2.

Validation against Grid-based Simulators: The proposed CEM model was compared against a standard commercial simulator. The CEM model captured the non-linear redirection of fluids with an RMSE for water-cut prediction of less than 4.2%, while reducing computational time by over 80%.

3.2. Field case

Based on the primary oil-bearing layers of a specific oilfield, a connection system was constructed using the point cloud triangulation method to establish a meshless water flow model. The key design metrics and operational configurations utilized to initialize this computational grid are systematically consolidated in **Table 5**. The model consists of 108 wells (46 injectors and 62 producers within one layer), 640 nodes, and 1,421 connections. This model accurately characterizes the distribution of initial transmissibility, initial connection volume, permeability, porosity, and initial oil saturation, as shown in **Figure 14**.

Table 5. Available construction parameters for the target offshore block model.

Item	Value
Model dimensionality	Single representative layer
Total wells	108
Injection wells	46
Production wells	62
Point-cloud nodes	640
Connections	1,421
Simulation period	4,200 days

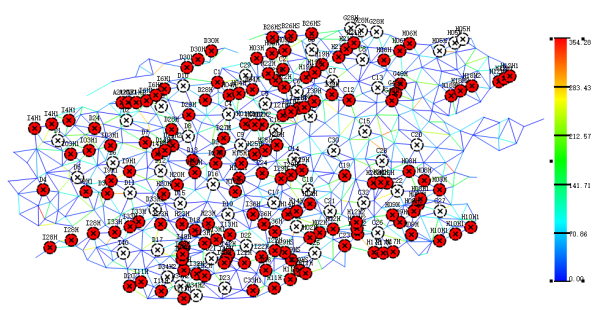

(a) Initial transmissibility distribution

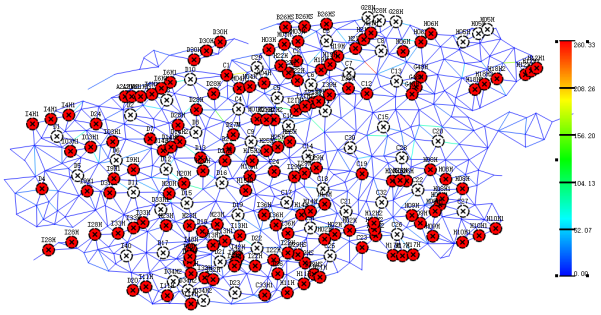

(b) Initial connection volume distribution

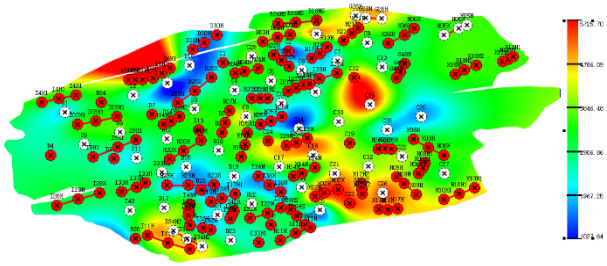

(c) Permeability distribution

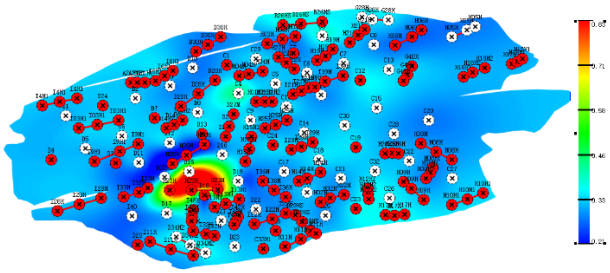

(d) Porosity distribution

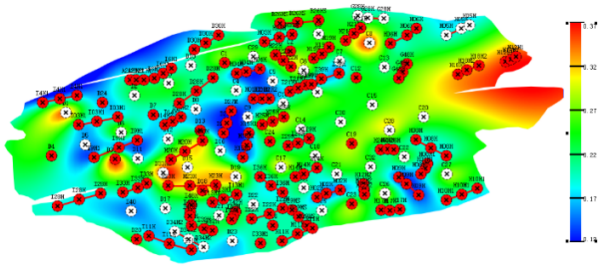

(e) Initial oil saturation distribution

Figure 14. Oilfield model parameters.

The dynamic simulation of the entire production life cycle for the offshore block was achieved, covering block cumulative oil production, block water cut, single-well daily oil production, single-well water cut, and oil-water saturation, as shown in **Figure 15**. From the overall block perspective, the cumulative oil production and water cut curves calculated by the model show high consistency with field-measured data, accurately reflecting the entire process of the block's water cut rising rapidly from 40% to over 90%. More importantly, regarding the characterization of single-well treatment effects, taking the typical well I28H (which underwent profile control) as an example, the water cut of this well once exceeded 95% during the mid-production stage, exhibiting typical high water-consumption characteristics. After the implementation of profile control measures, the measured water cut decreased to a minimum of approximately 20% and maintained a period of stable production with a low water cut for a considerable time.

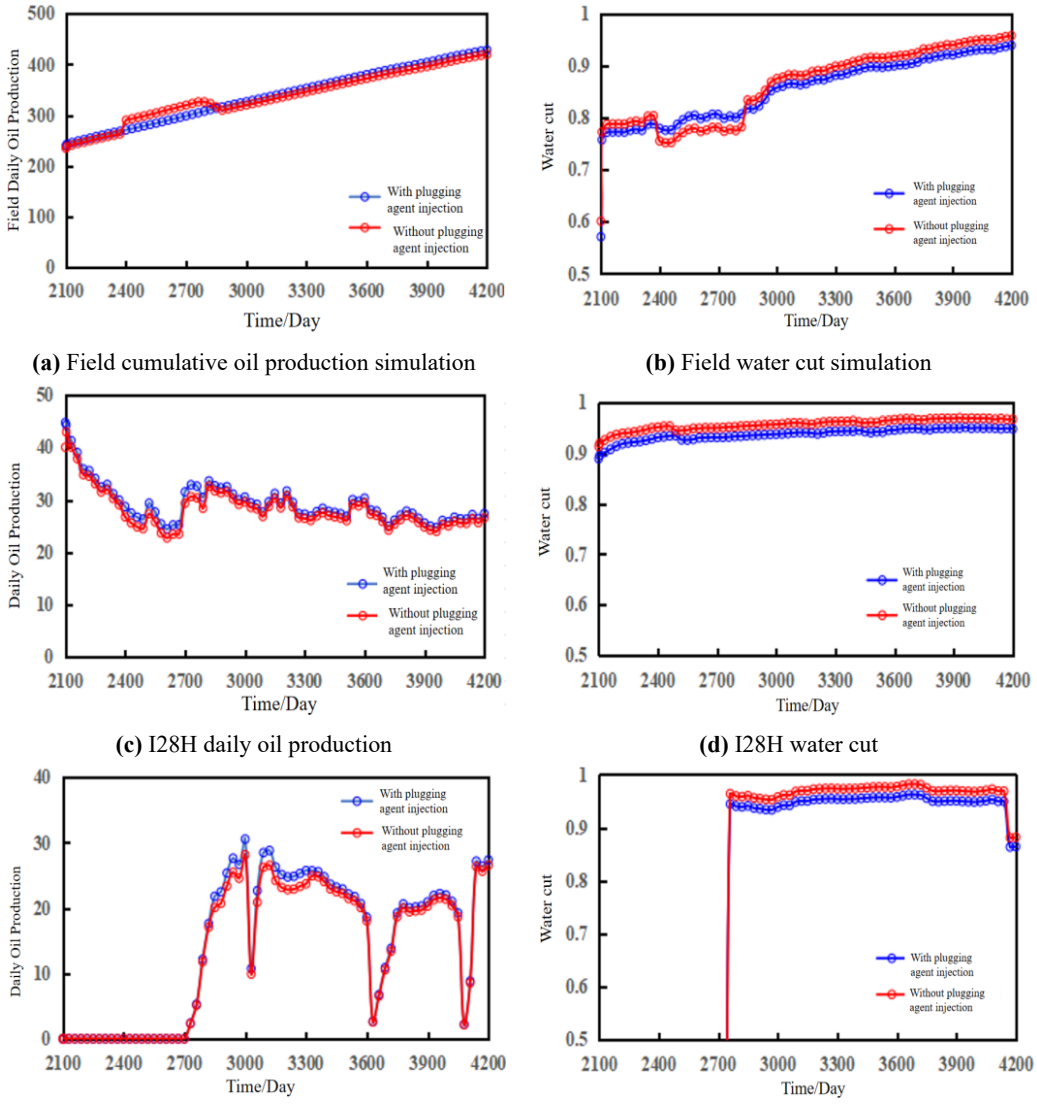

(a) Field cumulative oil production simulation

(b) Field water cut simulation

(c) I28H daily oil production

(d) I28H water cut

(e) H23H daily oil production

(f) H23H water cut

Figure 15. Production performance.

The meshless CEM simulation curves precisely captured this dramatic stepwise change. Meanwhile, the cumulative oil production curve exhibited a significant

inflection point with a sudden increase in slope. This confirms that the model can quantitatively reproduce the physical process of "plugging high-permeability layers—flow redirection—mobilizing low-permeability reserves" through the dynamic correction of permeability and rheology, providing a reliable numerical basis for the subsequent optimization of field IPC schemes based on this model.

Quantitative Error Metrics: Water Cut RMSE is approximately 3.8% across key production wells. Cumulative Oil Production Relative Error is less than 5.1%. Regarding computational efficiency, the meshless solver completed the 4,200-day simulation in minutes, outperforming conventional tools.

The split coefficients and preferential connectivity paths are shown in **Figure 16**. By comparing the distribution of preferential connectivity paths in **Figure 16c** and **Figure 16d**, it can be observed that before the implementation of measures, the internal flow field of the reservoir was primarily controlled by a small number of preferential channeling paths with high conductivity. The distribution of connectivity paths was sparse and concentrated, leading to the short-circuit circulation of injected water along fixed directions. After implementing IPC and flow field optimization measures, the network density of inter-well preferential connectivity paths increased significantly. The originally singular strong flow channels were dispersed, and the streamlines exhibited a more uniform and complex net-like distribution across the plane. This fundamental change in the flow field structure intuitively confirms that the deep plugging by chemical agents forced the injected fluid to undergo effective flow redirection. This successfully swept into the matrix regions with originally low displacement degrees, thereby substantially expanding the macroscopic sweep volume and achieving effective potential tapping of the remaining oil.

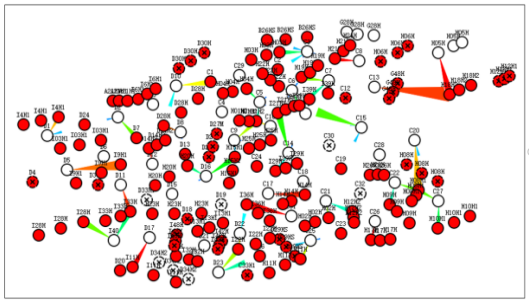

(a) Split coefficients before injection-production

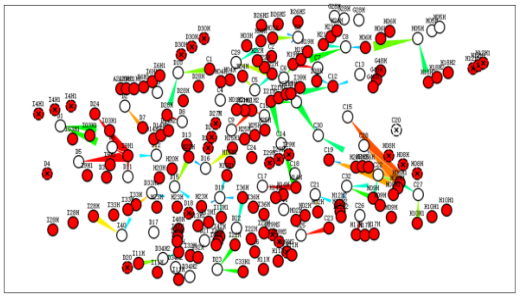

(b) Split coefficients after injection-production

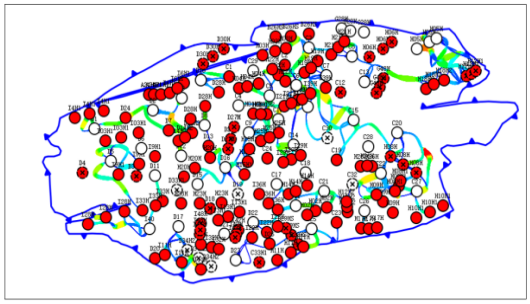

(c) Preferential connectivity paths before injection-production

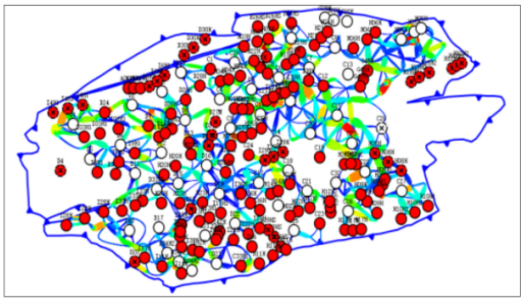

(d) Preferential connectivity paths after injection-production

Figure 16. Field flow paths.

Based on the color scale analysis in **Figure 16**, the red paths represent Level-I channeling channels with the strongest flow capacity and the most detrimental

impact on water injection performance, primarily corresponding to subsurface high-permeability zones with excellent connectivity. Yellow and green paths represent medium-strength channeling channels, while blue paths represent regions with slow flow velocities where fluids primarily move through the rock matrix. As observed from the field-wide distribution in **Figure 17a**, the distribution of preferential channels is highly non-uniform. Further observation of the localized close-ups for typical well groups such as G34H, H09H, and I4H1 clearly identifies several key red paths connecting injection and production wells. These red paths carry the vast majority of the ineffective water injection volume, causing the injected water to flow through directly without displacing oil. This classification result intuitively illustrates the primary destination of subsurface water flow and precisely pinpoints the specific locations requiring deep profile control. It provides a direct basis for formulating the subsequent treatment strategy: "Prioritize plugging red Level-I channels, auxiliary regulation of yellow strong channels, and forcing water flow into blue matrix regions.

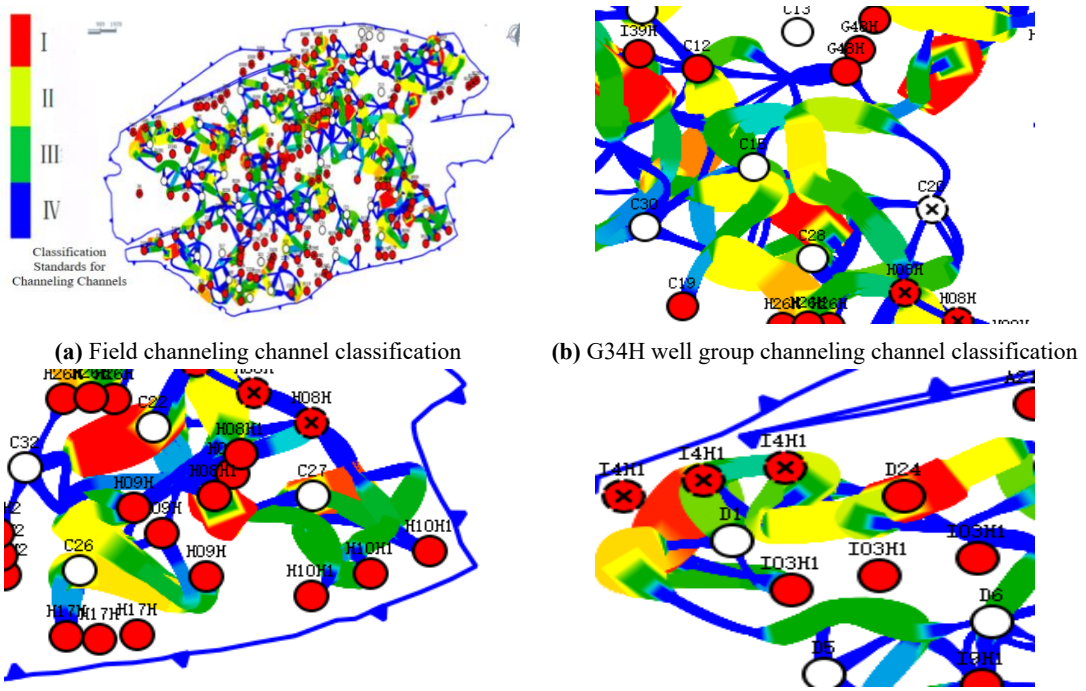

(a) Field channeling channel classification **(b)** G34H well group channeling channel classification

(c) H09H well group channeling channel classification **(d)** I4H1 well group channeling channel classification

Figure 17. Channeling channel classification map.

4. Results and discussion

To elucidate the underlying seepage mechanics responsible for the attenuation of connection transmissibility, it is essential to examine the micro-scale fluid-rock interactions during chemical agent injection. As the polymer or profile-control solutions propagate through the porous medium, the large macromolecules undergo both physical adsorption onto the rock matrix surfaces and mechanical entrapment within narrow pore throats. These hydrodynamic retention mechanisms continuously reduce the available cross-sectional area for fluid flow, manifesting macroscopically as a severe decline in absolute permeability. Because the injected chemical fluids preferentially invade high-conductivity thief zones characterized by minimal initial

flow resistance, this retention process is highly selective. Consequently, the observed transmissibility attenuation is inherently anisotropic, predominantly restricting the dominant channeling paths. This localized permeability reduction fundamentally alters the spatial distribution of flow resistance, establishing a dynamic pressure barrier. From a seepage mechanics perspective, this barrier forces the subsequent displacing fluid to divert into adjacent, previously unswept low-permeability regions, thereby effectively suppressing viscous fingering and improving the overall macroscopic sweep efficiency. Accurate identification and classification of channeling pathways are prerequisites for differentiated profile control and flooding. In the field application to the target offshore block, the proposed multi-parameter coupled identification method demonstrates excellent practical adaptability. By calculating the splitting coefficient and channeling factor for all connection elements, the complex inter-well network is quantitatively divided into four grades (Grade I to Grade IV). Grade I pathways (extreme channeling) are mainly distributed along the dominant flow directions between injectors and producers and correspond to high-permeability zones, which are highly consistent with fast water breakthrough directions observed from field monitoring data. This quantitative classification directly guides engineering design: Grade I channels require strong plugging materials such as high-strength gels, while Grade III and Grade IV zones are suitable for deeply migrating profile-control agents. This approach effectively eliminates the blindness commonly encountered in conventional profile modification operations.

Limitations: While advection-dominated assumptions are highly accurate for channeling environments, neglecting gravity and capillary forces limits the model's accuracy when applied to thick reservoirs with strong vertical heterogeneity or highly water-wet matrix zones where imbibition is dominant. Future iterations will integrate multi-phase capillary phase behaviors.

5. Conclusion

An integrated meshless numerical model for profile control and chemical flooding was developed, which explicitly couples fluid viscosity enhancement and dynamic rock adsorption. The model accurately captures flow diversion mechanisms with a 3.8% water-cut prediction RMSE, while providing a hierarchical mechanism to quantitatively identify and warn against dominant channeling pathways. By defining a dimensionless channeling factor based on multi-parameter integration, preferential seepage channels are quantitatively classified into four grades. This grading system provides a direct, objective decision-making basis for implementing differentiated profile control and targeted plugging treatments in mature oilfields.

In future research, we will further calculate oil increment and economic control indicators to quantitatively evaluate the economic feasibility and application value of the proposed optimization scheme. On this basis, systematic analysis will be conducted on key economic parameters, including operating costs, input-output ratio, and investment return cycle, so as to fully clarify the economic benefits and practical advantages of the optimization strategy in actual oilfield production. In addition, the research conclusions of this paper are summarized based on the geological conditions,

reservoir characteristics, and production modes of specific offshore oilfields, which have certain regional and scenario limitations. Therefore, we will further expand and deepen the current research results in subsequent studies. By investigating the differences in reservoir physical properties, fluid conditions, well pattern distribution, and production parameters among different types of oilfields, we will revise and improve the relevant optimization models and parameter adaptation rules, break the application restrictions of the existing research conclusions, and realize the popularization and adaptive application of the optimization method in more onshore and offshore oilfield production scenarios. The ultimate goal is to provide a universal, economical, and efficient technical reference for the optimal development and efficient production of various oilfields.

Author contributions: Methodology, WY, WZ (Wentao Zhan), WL and JM; software, WY, WZ (Wentao Zhan) and WL; formal analysis, WY, WZ (Wentao Zhan) and WL; investigation, WY, WZ (Wentao Zhan), WL, YZ and JM; writing—original draft preparation, all authors; supervision, ZW, JZ, WZ (Wensheng Zhou) and YL. All authors have read and agreed to the published version of the manuscript.

Funding: The project is supported by the Comprehensive Scientific Research Program of CNOOC Limited (KJZH-2024-2208) and the Natural Science Foundation of Xinjiang Uygur Autonomous Region (No. 2025D01B152), the Science and Technology Innovation Team Project of the Xinjiang Uygur Autonomous Region (Grant No. 2024TSYCTD0018). The China Postdoctoral Science Foundation (No. 2025M772960).

Institutional review board statement: Not applicable.

Informed consent statement: Not applicable.

Data availability statement: The data that support the findings of this study are available within the article.

Conflict of interest: No conflict of interest exists in the submission of this manuscript, and the manuscript is approved by all authors for publication. The authors would like to declare that the work described was original research that has not been published previously, and is not under consideration for publication elsewhere, in whole or in part. All the authors listed have approved the manuscript that is enclosed.

AI use statement: During the preparation of this manuscript, the authors used artificial intelligence tools solely for language refinement. No AI tools were used for data analysis, interpretation, or generation of scientific content. All outputs were critically reviewed and edited by the authors. The authors take full responsibility for the integrity and accuracy of the work.

References

1. Han D. Study on Accurate Prediction of Remaining Oil Relative Enrichment Zones to Enhance Waterflooding Recovery in Oilfields. Acta Petrolei Sinica, 2007; 28: 73–78.
2. Zhang S, Yu H, Wang Y, et al. Research on Displacement Technology for a Binary Heterogeneous System

in Fractured-Vuggy Reservoirs. Journal of Energy Engineering. 2026; 152(3): 04026018. doi: 10.1061/JLEED9.EYENG-6633
3. Nie X, Chen J, Cao Y, et al. Investigation on Plugging and Profile Control of Polymer Microspheres as a Displacement Fluid in Enhanced Oil Recovery. Polymers. 2019; 11(12): 1993. doi: 10.3390/polym11121993
4. Tong K, Song W, Chen H, et al. Automatic History Matching Method and Application of Artificial Intelligence for Fractured-Porous Carbonate Reservoirs. Processes. 2024; 12(12): 2634. doi: 10.3390/pr12122634
5. Kabir CS, Ismadi D, Fountain S. Estimating in-place volume and reservoir connectivity with real-time and periodic surveillance data. Journal of Petroleum Science and Engineering. 2011; 78(2): 258–266. doi: 10.1016/j.petrol.2011.05.017
6. Nagao M, Datta-Gupta A. Physics Informed Machine Learning for Reservoir Connectivity Identification and Production Forecastingfor CO2-EOR. In: Proceedings of the SPE Annual Technical Conference and Exhibition; 20 September 2024; New Orleans, LA, USA. doi: 10.2118/221057-MS
7. England WA. The organic geochemistry of petroleum reservoirs. Organic Geochemistry. 1990; 16(1–3): 415–425. doi: 10.1016/0146-6380(90)90058-8
8. Dinh A, Tiab D. Inferring Interwell Connectivity from Well Bottomhole-Pressure Fluctuations in Waterfloods. SPE Reservoir Evaluation & Engineering. 2008; 11(05): 874–881. doi: 10.2118/106881-PA
9. Ji Y, Zhang L. A method for analyzing interwell connectivity based on gated recurrent network with knowledge interaction. Frontiers in Earth Science. 2025; 13: 1678611. doi: 10.3389/feart.2025.1678611
10. Albertoni A, Lake LW. Inferring Interwell Connectivity Only From Well-Rate Fluctuations in Waterfloods. SPE Reservoir Evaluation & Engineering. 2003; 6(01): 6–16. doi: 10.2118/83381-PA
11. Ye H, Deng J, Ma J, et al. Interwell Connectivity Analysis Method Based on Injection–Production Data Time and Space Scale Coupling. Processes. 2025; 13(2): 373. doi: 10.3390/pr13020373
12. Yousef AA, Lake LW, Jensen JL. Analysis and Interpretation of Interwell Connectivity From Production and Injection Rate Fluctuations Using a Capacitance Model. In: Proceedings of the SPE/DOE Symposium on Improved Oil Recovery; 22 April 2006; Tulsa, OK, USA. doi: 10.2118/99998-MS
13. Moreno GA, Lake LW. On the uncertainty of interwell connectivity estimations from the capacitance-resistance model. Petroleum Science. 2014; 11(2): 265–271. doi: 10.1007/s12182-014-0339-0
14. Holanda RWD, Gildin E, Jensen JL, et al. A State-of-the-Art Literature Review on Capacitance Resistance Models for Reservoir Characterization and Performance Forecasting. Energies. 2018; 11(12): 3368. doi: 10.3390/en11123368
15. Male F. Pywaterflood: Well connectivity analysis throughcapacitance-resistance modeling. Journal of Open Source Software. 2024; 9(95): 6191. doi: 10.21105/joss.06191
16. Yuan G, Shangguan Y, Gao C, et al. Surfactant/Polymer Flooding Combined with Gel and Polymer Microsphere Plugging for Enhanced Oil Recovery in a Low-Permeability Reservoir. ACS Omega. 2026; 11(12): 19356–19368. doi: 10.1021/acsomega.5c12733
17. Mwangupili O, Pu C. Enhancing Oil Recovery in Vertical Heterogeneous Sandstone Reservoirs Using Low-Frequency Pulsating Water Injection. Processes. 2025; 13(2): 296. doi: 10.3390/pr13020296
18. Zhao H, Kang Z, Zhang X, et al. A Physics-Based Data-Driven Numerical Model for Reservoir History Matching and Prediction With a Field Application. SPE Journal. 2016; 21(06): 2175–2194. doi: 10.2118/173213-PA
19. Guo Z, Reynolds AC, Zhao H. A Physics-Based Data-Driven Model for History Matching, Prediction, and Characterization of Waterflooding Performance. SPE Journal. 2018; 23(02): 367–395. doi: 10.2118/182660-PA
20. Guo Z, Reynolds AC. INSIM-FT in three-dimensions with gravity. Journal of Computational Physics. 2019; 380: 143–169. doi: 10.1016/j.jcp.2018.12.016
21. Zheng Z, Chen S, An F, et al. A GIN-Based Pre-Identification Method for Dominant Flow Channels in Connection-Element Reservoirs: An Optimized Ant Colony Algorithm Search Scheme. Processes. 2026; 14(10): 1605. doi: 10.3390/pr14101605
22. Pope GA, Nelson RC. A Chemical Flooding Compositional Simulator. Society of Petroleum Engineers Journal. 1978; 18(05): 339–354. doi: 10.2118/6725-PA
23. Delshad M, Pope GA, Sepehrnoori K. A compositional simulator for modeling surfactant enhanced aquifer remediation, 1 formulation. Journal of Contaminant Hydrology, 23(4): 303–327. doi: 10.1016/0169-7722(95)00106-9
24. Thiele MR, Batycky RP, Blunt MJ. A Streamline-Based 3D Field-Scale Compositional Reservoir Simulator. In: Proceedings of the SPE Annual Technical Conference and Exhibition; 5 October 1997; San Antonio, TX, USA. doi: 10.2118/38889-MS

25. Datta-Gupta A, King MJ. Streamline Simulation: Theory and Practice. Society of Petroleum Engineers; 2007. doi: 10.2118/9781555631116
26. Sayarpour M, Zuluaga E, Kabir CS, et al. The use of capacitance–resistance models for rapid estimation of waterflood performance and optimization. Journal of Petroleum Science and Engineering. 2009; 69(3–4): 227–238. doi: 10.1016/j.petrol.2009.09.006
27. Singh KG, Pathania T. Development and real field application of meshless generalized finite difference method for unconfined groundwater flow modelling. Mathematics and Computers in Simulation. 2026; 240: 332–346. doi: 10.1016/j.matcom.2025.07.027
28. Tang Z, Pan H, Fu Z, et al. A least-squares generalized finite difference method for solving nonlinear reaction–diffusion systems. Engineering Analysis with Boundary Elements. 2025; 179: 106351. doi: 10.1016/j.enganabound.2025.106351
29. Rao X, He X, Du K, et al. A Novel Projection-based Embedded Discrete Fracture Model (pEDFM) for Anisotropic Two-phase Flow Simulation Using Hybrid of Two-point Flux Approximation and Mimetic Finite Difference (TPFA-MFD) Methods. Journal of Computational Physics. 2024; 499: 112736. doi: 10.1016/j.jcp.2023.112736
30. Zhao H, Zhan W, Yuhui Z, et al. A connection element method: Both a new computational method and a physical data-driven framework—Take subsurface two-phase flow as an example. Engineering Analysis with Boundary Elements. 2023; 151: 473–489. doi: 10.1016/j.enganabound.2023.03.021
31. Tarjan R. Depth-First Search and Linear Graph Algorithms. SIAM Journal on Computing. 1972; 1(2): 146–160. doi: 10.1137/0201010
32. Zhou Y, Wang L, Shi M, et al. Dynamic connectivity analysis of fracture-vuggy reservoir based on meshless method. Geoenergy Science and Engineering. 2025; 246: 213602. doi: 10.1016/j.geoen.2024.213602